

Article

Tandem effect of Ag@C@Cu catalysts enhances ethanol selectivity for electrochemical CO₂ reduction in flow reactorsJie Zhang,^{1,2} Thi Ha My Pham,^{1,2} Youngdon Ko,^{1,2} Mo Li,^{1,2} Shuliang Yang,³ Cedric David Koolen,^{1,2} Liping Zhong,^{1,2} Wen Luo,^{4,5,*} and Andreas Züttel^{1,2}

SUMMARY

CO-selective metals (e.g., Ag) on Cu catalysts improve the selectivity of multi-carbon (C₂₊) products in electrochemical CO₂ reduction. However, the origin of the improvement remains unclear due to the convolution of tandem and interface effects. Here, Ag@C@Cu core-shell catalysts were synthesized, in which the thin carbon interlayer inhibited the direct interaction between Ag and Cu while still allowing the reduction of CO₂ on Ag, thus isolating the tandem effect from other effects. This catalyst produced higher ratios of ethanol to ethylene relative to the monometallic Cu catalyst, demonstrating that the locally increased CO concentration promoted the ethanol pathway over the ethylene pathway. Further, the selectivity of ethanol was optimized by tuning the thickness of the Cu shell. This work provides a rational approach to design core-shell catalysts for understanding structure-performance relationships and demonstrates the key role of the tandem effect in tuning the selectivity of C₂₊ products.

INTRODUCTION

Electrochemical CO₂ reduction (CO₂RR) is one of the most promising technologies that can produce commodity chemicals by using renewable electricity as an energy source.¹ However, the selectivity and energy efficiency of producing C₂₊ molecules, e.g., ethylene (C₂H₄) and ethanol (C₂H₅OH), are still too low to make this technology industrially viable,² with a key constraint being the lack of advanced electrocatalysts.^{3–5} Currently, Cu is the only metal catalyst capable of catalyzing CO₂RR to produce C₂₊ molecules; however, it has insufficient selectivity for practical applications. Thus, various approaches have been developed to engineer Cu materials to improve the selectivity and activity toward C₂₊ products.^{3,6} Among these approaches, introducing a CO-selective metal (e.g., Ag) to Cu catalysts has emerged as an effective approach.^{7–13}

The selectivity enhancement of Ag-Cu bimetallic catalysts for CO₂RR to C₂₊ products has been ascribed to the tandem effect, in which Ag and Cu work sequentially as different active sites, i.e., the Ag surface first converts CO₂ molecules to CO; these CO molecules then diffuse to the Cu surface and are further reduced to C₂₊ products.^{10,12,14,15} In practice, Ag-Cu catalysts prepared by conventional methods, such as co-electrodeposition,¹⁰ co-physical vapor deposition,¹¹ sequential precipitation,^{13,16–19} galvanic replacement,^{9,12} and physical blending,²⁰ inevitably contain interfaces between Ag and Cu, where Ag atoms are in direct contact with Cu atoms.^{11,21,22} The dynamic reconstruction of both Ag and Cu surfaces during

¹Laboratory of Materials for Renewable Energy (LMER), Institute of Chemical Sciences and Engineering (ISIC), Basic Science Faculty (SB), École Polytechnique Fédérale de Lausanne (EPFL) Valais/Wallis, Energypolis, Rue de l'Industrie 17, 1951 Sion, Switzerland

²Empa Materials Science & Technology, 8600 Dübendorf, Switzerland

³College of Energy, Xiamen University, Xiang'an South Road, Xiamen 361102, China

⁴School of Environmental and Chemical Engineering, Shanghai University, 99 Shangda Road, Shanghai 200444, China

⁵Lead contact

*Correspondence: wenluo@shu.edu.cn
<https://doi.org/10.1016/j.xcrp.2022.100949>



CO₂RR may further increase the possibility of incorporating Ag atoms into Cu-surface layers.^{23,24} These interface sites can also improve the selectivity of C₂₊ products (e.g., C₂H₄ and C₂H₅OH) due to changes in electronic structures relative to those of the pristine Cu surface,^{11,22} thus leading to an indeterminate reaction mechanism.¹³ For example, several previous studies have reported that Ag-Cu catalysts improved C₂H₄ selectivity, while others found that C₂H₅OH production was favored.^{10,11,13,15,16} The co-existence of both tandem and interface effects in these Ag-Cu catalysts resulted in the ambiguity of these findings and makes it challenging to ascertain how each effect alone affects the production of C₂H₄ and C₂H₅OH. The equivocal nature of these findings highlights the importance of deconvoluting the tandem and interface effects to reveal their influence on reaction pathways.

Though sophisticated physical methods (e.g., photolithography) can be used to produce bimetallic electrodes with tandem structures, the limited surface area of these catalysts makes them suitable only as model catalysts for CO₂RR at low current densities.¹⁵ As CO₂RR performance is known to be highly sensitive to the local reaction environment,^{5,25–27} catalysts should accordingly be developed and optimized for practical-application conditions. This calls for the use of flow reactors,^{25,28} since the flow configuration combined with gas-diffusion electrodes allow continuous reaction processes at high current densities and have been widely used for different electrochemical-synthesis processes.^{29,30}

In order to deconvolute the tandem and interface effects and to more rationally design Ag-Cu catalysts with higher selectivity for CO₂RR to C₂₊ products, in this work, we designed and synthesized Ag@C@Cu core-shell nanoparticles (NPs) comprising an Ag core and a Cu shell separated by a carbon interlayer. The presence of the carbon layer prevented the formation of Ag-Cu interfaces but still allowed the reduction of CO₂ molecules to CO on the Ag core. We tested these samples in a flow reactor at current densities of up to 400 mA cm⁻² and found that with only the tandem effect, the selectivity of C₂H₅OH was enhanced compared with that of C₂H₄. Furthermore, we demonstrated that the product selectivity was adjustable by altering the thickness of the Cu shell: while the C₂H₄ selectivity decreased with decreasing the Cu-shell thickness, the C₂H₅OH selectivity was maximized at an optimal Cu-shell thickness.

RESULTS AND DISCUSSION

Synthesis and characterization of Ag@C@Cu catalysts

To avoid direct contact between Ag and Cu, we attempted to prepare Cu-Ag catalysts with a core-shell structure of Ag core, thin carbon interlayer, and Cu shell, namely Ag@C@Cu. Carbon was selected to be an interlayer due to its chemical inertia and good electrical conductivity.^{15,31,32} Notably, the carbon interlayer must be intact, and the layer thickness must be as thin as possible to ensure that the Ag core remains accessible to the CO₂ and the electrolyte.³¹ Accordingly, the synthesis procedure of the Ag@C@Cu core-shell structure was carefully designed. [Figures 1](#) and [S1](#) show a schematic illustration of the synthesis process of the Ag@C@Cu catalyst, including the corresponding transmission electron microscopy (TEM) images for the intermediate materials.

The synthesis process began with the synthesis of Ag NPs of ca. 59 ± 13 nm ([Figures S2](#) and [S3A](#)) by reducing AgNO₃ with glucose. A layer of polydopamine (PDA; ~4 nm thick), as the precursor of the carbon layer, was then grown on the Ag NPs to form Ag@PDA NPs through polymerizing free dopamine. The Ag@PDA

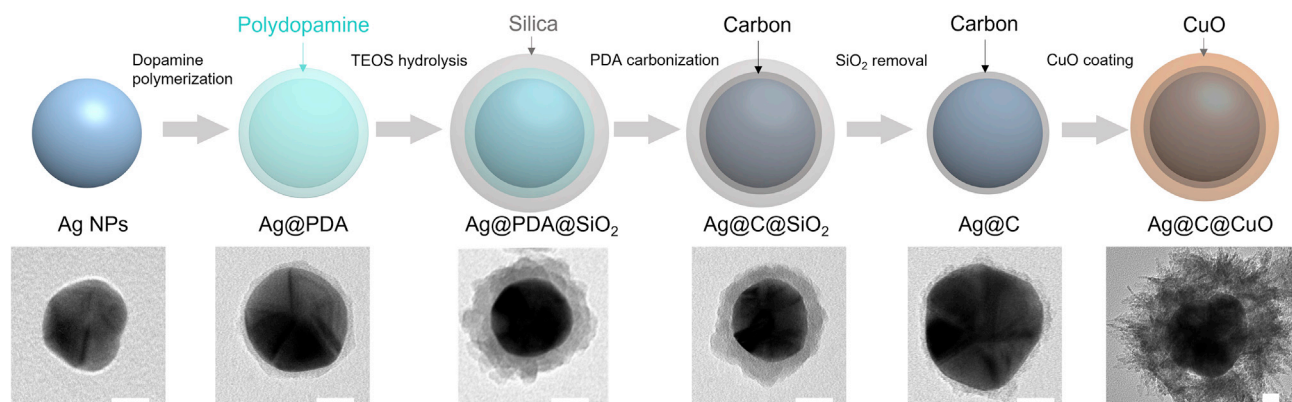


Figure 1. Schematic of the synthesis procedure of Ag@C@Cu core-shell NPs and the corresponding TEM images of representative individual particles in each step

The scale bar in each image is 20 nm. See also Figures S1–S5.

NPs were further coated by a layer of silica (~ 8 nm thick) to form Ag@PDA@SiO₂ NPs by hydrolyzing tetraethoxysilane. The Ag@PDA@SiO₂ NPs were annealed at 700°C under nitrogen to carbonize the PDA layer. The presence of the SiO₂ layer prevented both the agglomeration of NPs (Figure S6) and the exfoliation of the carbon layer during the carbonization of PDA. The as-formed Ag@C@SiO₂ NPs were treated with a solution of NaOH and diethylamine to remove the SiO₂ layer to obtain the Ag@C core-shell samples.

To coat a Cu layer, the Ag@C NPs were first coated with a layer of polyvinylpyrrolidone (PVP) to increase the hydrophilicity of the sample. The Cu₂O layer was then grown on the Ag@C NPs in the Cu(NO₃)₂ solution with ascorbic acid as the reducing agent, and the mass ratio of Cu to Ag was controlled to be 1. The Cu₂O layer was finally oxidized by air in an ammonia solution in C₂H₅OH to obtain Ag@C@CuO NPs. Using this oxidation method, an intact Cu₂O layer was converted to a porous CuO layer, which not only increased the accessibility of CO₂ to the Ag core but also increased the chance of capturing CO intermediate by the Cu shell. During CO₂RR, the Ag@C@CuO NPs were reduced *in situ* to be Ag@C@Cu catalysts.

The layers of PDA, SiO₂, carbon, Cu₂O, and CuO involved in the synthesis of Ag@C@Cu are clearly observed in the TEM images in Figures 1 and S3–S5, in addition to the energy-dispersive X-ray spectroscopy (EDX) elemental maps shown in Figures 2D, 2E, S7, and S8. The carbon layer on the Ag@C core-shell was amorphous with a thickness of around 4 nm, as shown in the high-resolution TEM (HRTEM) image in Figure 2A. This carbon layer compactly wrapped the Ag surface, preventing direct growth of the Cu layer on the Ag surface. A clear gap is visible between the Ag core and the Cu shell in the TEM image in Figure 2B, demonstrating that this carbon layer is stable during the deposition and oxidation of the Cu₂O layer. The presence of the carbon layer is further confirmed by the Raman spectrum of Ag@C@CuO (Figure 2G), where clearly observed are the peaks at 1,360 and 1,580 cm^{−1}, corresponding to the D band and the G band of carbon, respectively.³³ In the EDX elemental maps and the corresponding energy spectra of Ag@C@CuO (Figures 2D–2F), the Ag core region showed a higher carbon signal density than that of the Cu-shell region, confirming the carbon layer wrapping the Ag core in the Ag@C@CuO NPs.

As shown in Figures 2B and S15, the CuO-shell layer has a porous structure composed of CuO needles. The HRTEM images and the corresponding diffraction

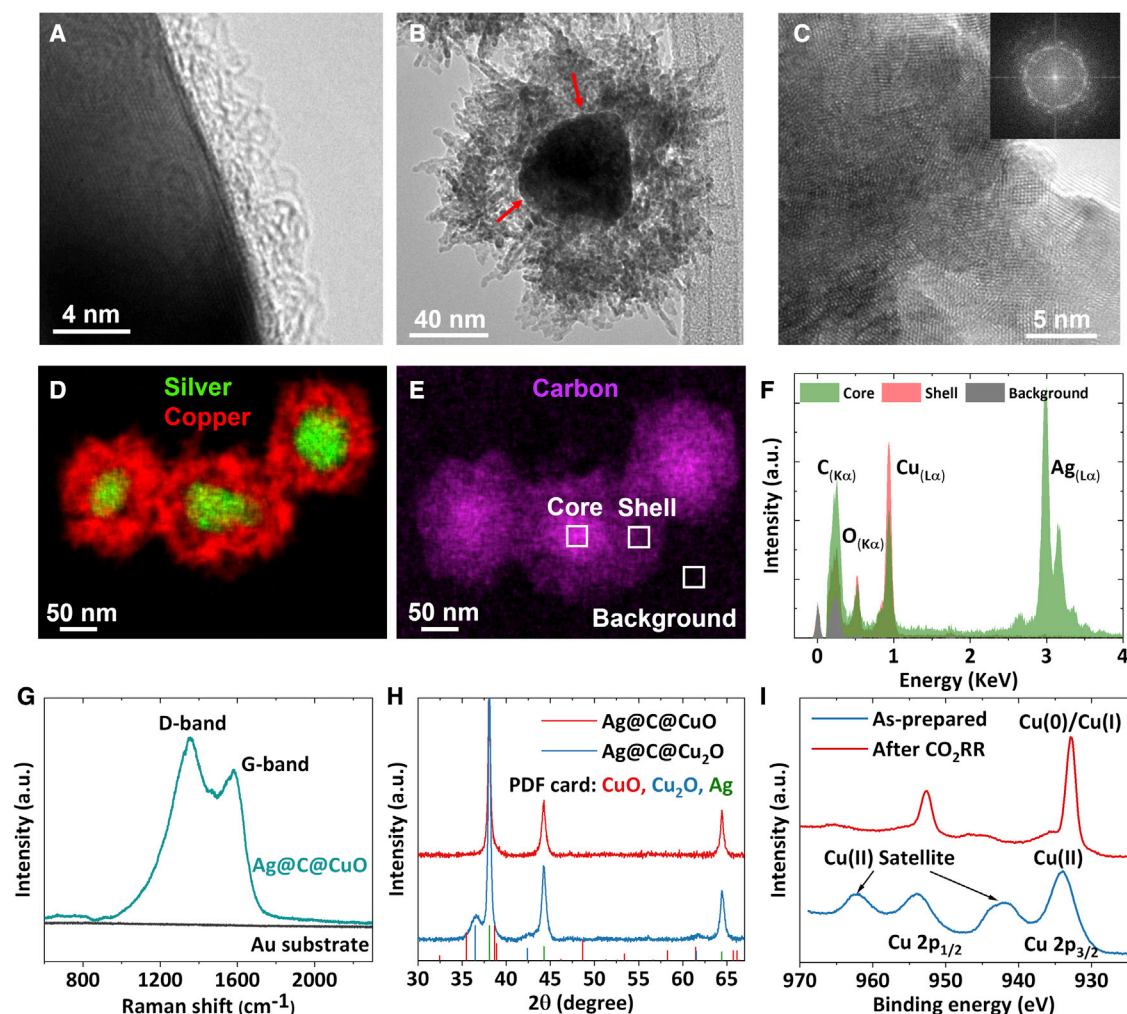


Figure 2. Characterization of Ag@C@CuO NPs

(A) HRTEM image of the carbon layer on Ag@C NPs.

(B) TEM image of a representative Ag@C@CuO NP.

(C) HRTEM image of the CuO layer in Ag@C@CuO NPs with an inset illustrating the corresponding diffraction pattern obtained by fast Fourier transform.

(D and E) EDX elemental maps of Cu, Ag, and carbon in Ag@C@CuO NPs.

(F) EDX spectra of the selected regions, corresponding to the core and shell of Ag@C@CuO NPs and the grid background, in the EDX elemental map (E).

(G) Raman spectra of Ag@C@CuO NPs deposited on an Au substrate.

(H) XRD patterns of Ag@C@Cu₂O and Ag@C@CuO NPs.

(I) Cu₂p XPS of Ag@C@Cu₂O NPs before and after CO₂RR.

See also [Figures S7–S11](#).

patterns obtained using the fast Fourier transform ([Figure 2C](#)) indicate that these CuO needles are assembled by CuO NPs with a high density of grain boundaries. As grain boundaries are proven to be active for C–C coupling, we expect that such a porous CuO layer would facilitate the conversion of CO generated from the Ag core.^{34,35} No Ag signal was detected in the Cu-shell region based on the EDX elemental maps and spectra ([Figures 2D–2F](#)), indicating that the Ag core was stable and did not migrate through the carbon layer during the sample synthesis. A comparison between the X-ray diffraction (XRD) patterns of Ag@C@Cu₂O and Ag@C@CuO in [Figures 2H](#) and [S9](#) confirms the complete conversion of Cu₂O to CuO, as no Cu₂O peak was observed in the XRD pattern of Ag@C@CuO. The broad

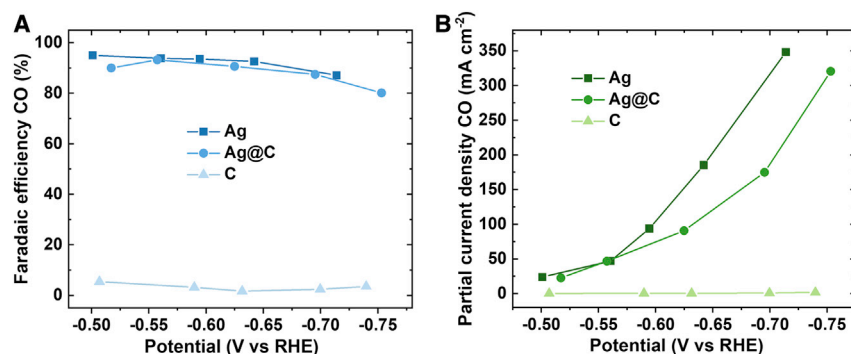


Figure 3. CO₂RR performance of Ag, C, and Ag@C NPs

(A) CO FE versus applied potential on Ag, C, and Ag@C NPs.

(B) CO partial current density versus applied potential on Ag, C, and Ag@C NPs.

XRD peak corresponding to CuO (Figures 2H and S9) also demonstrates that the CuO shell consisted of small grains, consistent with the HRTEM results. Much stronger diffraction peaks were observed for Ag, owing to the better crystallinity of the Ag core than that of the CuO shell. However, in the X-ray photoelectron spectroscopy (XPS) spectra, Cu showed a much stronger peak than Ag with a surface Cu/Ag atomic ratio of 132 (Figure S10A), indicating that the Ag core was well wrapped by the carbon layer and the Cu shell, as XPS has a limited information depth (~ 3.0 nm for Cu 2p, ~ 4.8 nm for Ag 3d, and ~ 9.9 nm for C 1s). The Cu 2p XPS spectra (Figure 2I) of Ag@C@CuO before CO₂RR showed a peak at 933.6 eV that can be assigned to Cu(II). After CO₂RR, a peak at 932.7 eV corresponding to Cu(0)/Cu(I) can be observed, demonstrating that the CuO shell was reduced to Cu(0)/Cu(I) during the CO₂RR process. Notably, the Cu(I) species possibly arose from the oxidation of the metallic Cu shell during the sample transfer.

After reduction under the CO₂RR condition, the needle structure of the CuO shell disappeared due to the structural reconstruction; however, the Cu shell remained porous (Figure S11). The reconstruction of Cu driven by CO₂RR has been widely reported and has been found to be related to the reduction potential and the adsorption of CO.^{24,36–39} Importantly, both the carbon layer and the core-shell structure remained intact after CO₂RR (Figure S11), indicating the viability of this core-shell catalyst for investigating the tandem effect in CO₂RR.

CO₂RR performance

The CO₂RR performance of all catalysts was evaluated in a flow cell at industrially relevant current densities with 1.0 M KOH as the electrolyte. The gas products were detected and quantified online using gas chromatography, and liquid products were quantified using ¹H nuclear magnetic resonance. Before undertaking performance testing of the Ag@C@Cu catalyst, we first explored the effect of the carbon layer on the CO₂RR performance of Ag. Carbon sphere particles (Figure S12), synthesized from the carbonization of PDA, were used as a reference sample. As shown in Figure 3A, this sample showed almost no activity for CO₂RR, suggesting a negligible activity contribution from the carbon interlayer in Ag@C@Cu. On the other hand, both Ag NPs and Ag@C NPs are highly selective for CO₂RR, showing around 90% Faradaic efficiency (FE) for CO in the potential range from -0.5 to -0.75 V vs RHE (Figure 3A). The partial current density of CO on the Ag@C NPs was smaller than that on the Ag NPs (Figure 3B) because the carbon layer can partially block the Ag sites. Nonetheless, these results demonstrate that the carbon interlayer does allow CO₂

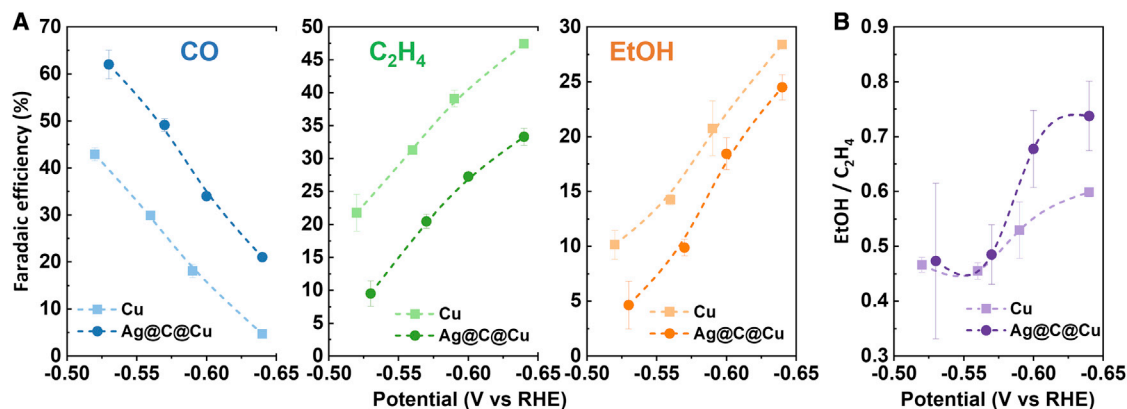


Figure 4. CO₂RR performance of Cu and Ag@C@Cu NPs

(A) FEs of CO, C₂H₄, and C₂H₅OH from CO₂RR on Cu and Ag@C@Cu at various potentials in a flow cell with 1.0 M KOH as the electrolyte. Data are represented as mean \pm SD.

(B) The ratios of C₂H₅OH FE to C₂H₄ FE on Cu and Ag@C@Cu. Data are represented as mean \pm SD.

See also Figure S13.

molecules to reach the surface of the Ag core. Despite being lower than that of pristine Ag NPs, the CO partial current density of Ag@C NPs still exceeded 300 mA cm⁻² at -0.75 V vs RHE, which is expected to provide sufficient CO for the Cu shell to establish the tandem effect.

To demonstrate the tandem effect in the Ag@C@Cu catalyst for CO₂RR, we prepared a control Cu NP sample via a similar synthesis method to that described above but without the Ag@C core. CO, C₂H₄, and C₂H₅OH were the three main products from CO₂RR over pure Cu and Ag@C@Cu catalysts (Figures 4 and S13). As shown in Figure 4, Ag@C@Cu showed higher FEs for CO but lower FEs for C₂H₄ and C₂H₅OH than the Cu sample. We interpret that the CO molecules generated from the Ag core were not completely captured and reduced by the Cu shell under our experimental conditions, probably because the Cu shell was too thin or too porous. As it is still debated whether the tandem effect enhances the selectivity of C₂H₄ or C₂H₅OH, we compared the C₂H₅OH/C₂H₄ ratios of the two samples. As shown in Figure 4B, the C₂H₅OH/C₂H₄ ratio on Ag@C@Cu was similar to that on Cu at potentials from -0.52 to -0.57 vs RHE. However, at more negative potentials from -0.60 to -0.64 V vs RHE, the ratio was much larger on Ag@C@Cu. Because no Ag–Cu interface was present in this Ag@C@Cu catalyst, the increased C₂H₅OH/C₂H₄ ratio should be ascribed exclusively to the increased local CO concentration from CO₂ reduction on Ag core—that is, the tandem effect. Therefore, these results demonstrate that the tandem effect favors the production of C₂H₅OH more than C₂H₄ and thus has the potential to be used to improve the selectivity of C₂H₅OH.

As Ag and Cu play different roles in converting CO₂ in a tandem catalytic system, we anticipated that the product distribution can be effectively tuned by changing the ratio of Ag and Cu in our core-shell catalysts. To verify this, we synthesized a series of Ag@C@Cu samples with Ag/Cu mass ratios of 0.1–1. These samples were prepared with the same Ag@C core, while the thickness of the Cu shell was controlled by changing the amount of Cu. As shown in Figure 5A, the Ag/Cu mass ratios determined by inductively coupled plasma optical emission spectroscopy (ICP-OES) is in good agreement with the mass ratios of the precursors added during the synthesis, demonstrating the accuracy and controllability of this method. Scanning electron

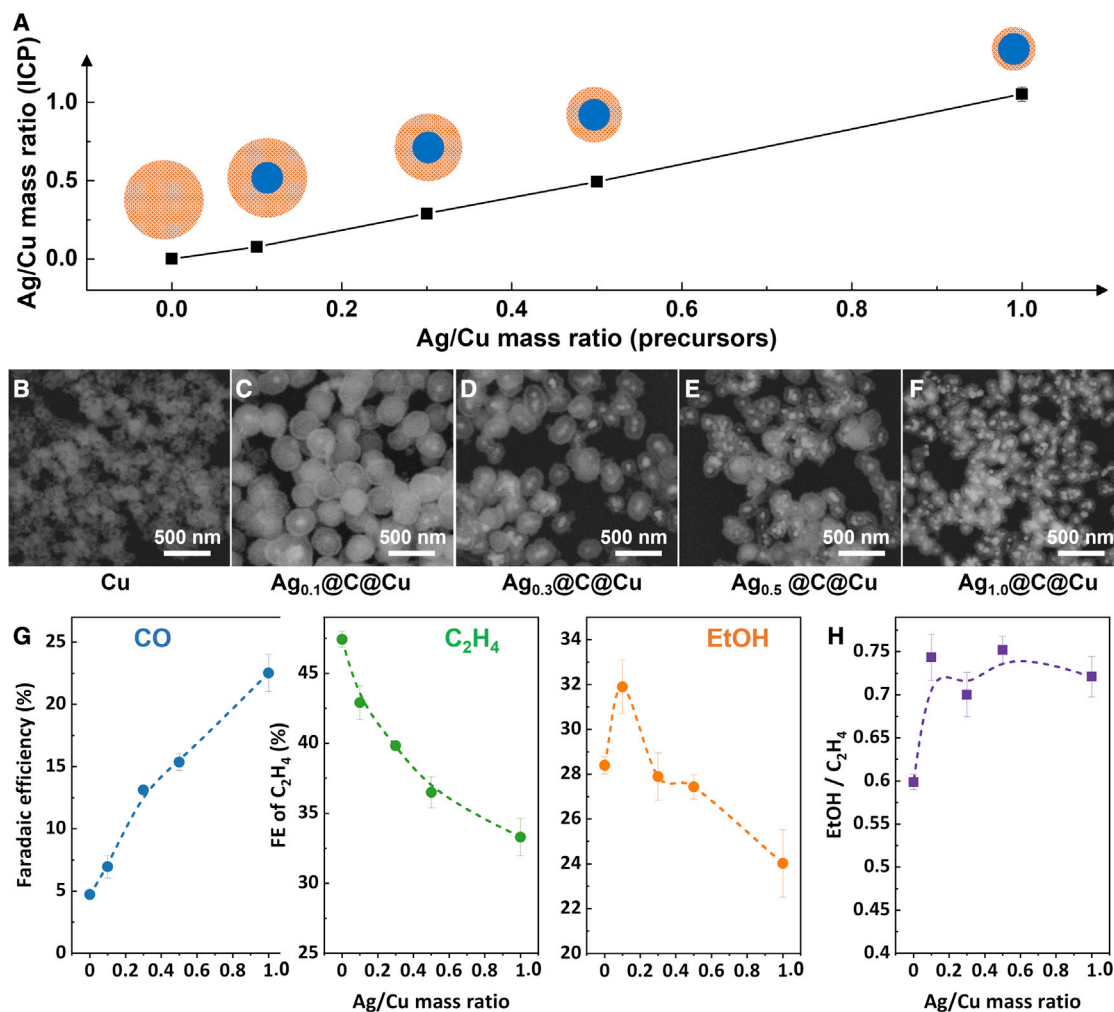


Figure 5. CO₂RR performance of Ag@C@Cu with different Cu shell thicknesses

(A) Ag/Cu mass ratio in Ag@C@Cu NPs determined by ICP-OES versus by precursors, with corresponding schematics of different samples. (B–F) Backscattered SEM images of Cu NPs and Ag@C@Cu NPs with various thicknesses of Cu shell. The mass ratios of Ag to Cu in the core-shell NPs in (C)–(F) are 0.1, 0.3, 0.5, and 1, respectively. (G) FEs of CO, C₂H₄, and C₂H₅OH from CO₂RR on Cu and Ag@C@Cu with various mass ratios of Ag to Cu at 400 mA cm⁻² (around -0.64 V vs RHE) in a flow cell with 1.0 M KOH as the electrolyte. Data are represented as mean ± SD. (H) The ratios of C₂H₅OH FEs to C₂H₄ FEs on Cu and Ag@C@Cu. Data are represented as mean ± SD. See also Figures S15–S18.

microscopy (SEM) and TEM images (Figures 5C–5F and S15–S17) also confirmed that with the mass ratios of Ag/Cu increasing from 0.1 to 1, the thickness of the Cu shell decreased gradually from around 90 to 40 nm.

We then evaluated these samples at 400 mA cm⁻² (corresponding to around -0.64 V vs RHE) in a flow cell with 1.0 M KOH as the electrolyte. The FEs of CO, C₂H₄, and C₂H₅OH on the Ag@C@Cu samples as a function of the Ag/Cu mass ratio are shown in Figure 5G. As predicted, the C₂H₄ FE continuously decreased with decreasing the Cu-shell thickness, and, in turn, the CO FE increased continuously. This can be attributed to two factors: (1) the increased amount of Ag relative to Cu promoted the CO production rate, and (2) the decreased Cu thickness limited the capture and conversion of CO molecules.⁴⁰ In contrast, the C₂H₅OH FE was maximized at an Ag/Cu ratio of 0.1, reaching a value of 31.5%, with a partial current density of 126 mA cm⁻².

The ratio of C_2H_5OH to C_2H_4 also increased from 0.6 for Cu to 0.74 for $Ag_{0.1}@C@Cu$ and plateaued at around 0.72 with a further increase in the Ag/Cu ratio (Figure 5H). These results again demonstrate that the selectivity of C_2H_5OH can be improved by the tandem effect between Ag and Cu and optimized by tuning the relative amount of Ag to Cu.

In addition, we performed control experiments over Ag@Cu catalysts synthesized by the same method to further understand the effect of the carbon interlayer on CO_2RR (Figures S19 and S20). Compared with Ag@C@Cu, Ag@Cu exhibited lower C_2H_4 and C_2H_5OH FE_s but higher CO FE_s and C_2H_5OH/C_2H_4 ratios. This can be attributed to the fact that the Ag core in Ag@Cu is more active for producing CO than that in Ag@C@Cu (Figure 3B). The high CO activity of Ag@Cu led to decreased FE_s for C_2H_4 and C_2H_5OH but increased $*CO$ coverage on the Cu shell, which resulted in a high C_2H_5OH/C_2H_4 ratio; details will be discussed below. Notably, as mentioned in the introduction, without separating Cu and Ag, we cannot exclude the possible effect of the Ag–Cu interface in Ag@Cu.

Mechanistic investigation

For bimetallic catalysts, it is always challenging to decouple the influence of geometric and electronic effects on their catalytic behavior.⁴¹ The underlying mechanism is even more complicated for Cu–Ag-based CO_2RR catalysts since the electron transfer, binding-site diversity, oxidation state, and tandem effect have all been proposed to play roles in reducing CO_2 .^{11,23,41,42} As we have shown that the Ag@C@Cu core-shell catalysts could isolate the tandem effect from other effects (Figure 6C), in this part, we discuss how the tandem effect improves the activity and selectivity of C_2H_5OH compared with C_2H_4 by combining previously published experimental and theoretical results with our results obtained from the well-defined core-shell catalysts.

First, we estimated the CO production rate by assuming all C_{2+} products and CH_4 are derived from the $*CO$ intermediate. This assumption is considered reasonable as $*CO$ is widely accepted as an intermediate of these products.³ We found that Ag@C@Cu produced CO at a higher rate than Cu (Figures 6A and S14), which confirmed the higher local concentration of CO in the vicinity of Ag@C@Cu relative to that of the pure Cu catalyst. To understand how the CO-rich environment would affect the reaction activity toward C_{2+} products, we normalized the partial current densities of C_{2+} , C_2H_4 , and C_2H_5OH by the mass of Cu in the electrode (Figure S14B). As expected, normalized C_{2+} production rates for Ag@C@Cu catalysts with different Ag/Cu ratios were around 20% higher than that for Cu, demonstrating the enhanced activity of Cu in a tandem catalytic system. Unexpectedly, the $Ag_{0.1}@C@Cu$ sample showed the highest normalized C_{2+} production rate, even though its local CO concentration was lower than the other Ag@C@Cu catalysts. We rationalize this result to a competition between Ag and Cu: under a similar reaction condition (i.e., 400 mA cm^{-2} at around -0.64 V), the more Ag involved in reducing CO_2 to CO, the less Cu is involved in reducing CO_2 and CO to C_{2+} . Therefore, a proper ratio of Ag/Cu is required in a tandem system to provide sufficient CO for C–C coupling while avoiding the excessive competition of the CO_2 -to-CO reaction. Further, we found that the enhanced C_{2+} partial current density over Ag@C@Cu catalysts was mainly contributed by the enhanced C_2H_5OH production (Figure 6B), again demonstrating that the reaction pathways toward C_2H_5OH are more favored than those toward C_2H_4 over this tandem system.

On the basis of several research groups' theoretical calculations, a high $*CO$ coverage can significantly affect the reaction pathways toward different C_{2+}

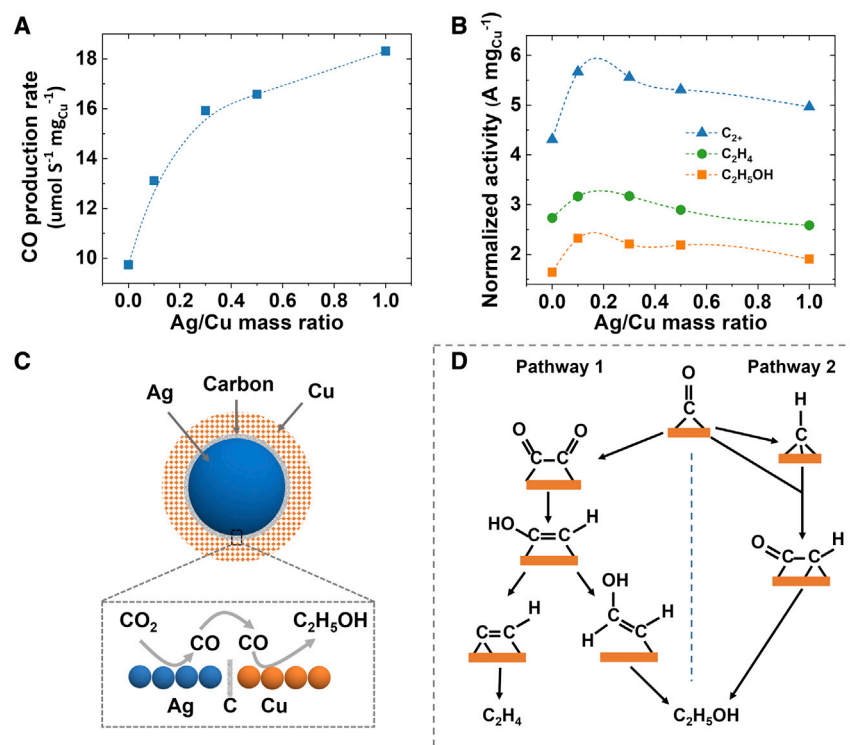


Figure 6. The reaction pathways for C₂H₅OH and C₂H₄

(A) CO production rate normalized by Cu mass in Cu and Ag@C@Cu NPs with an assumption that all C₂₊ products and CH₄ have *CO as the intermediate. The CO₂RR was evaluated at 400 mA cm⁻² in a flow cell with 1.0 M KOH as the electrolyte.

(B) The normalized partial activities of C₂H₅OH, C₂H₄, and C₂₊ on Ag@C@Cu NPs. The normalized partial activity refers to the partial current density divided by the Cu mass in the electrode.

(C) Schematics of the tandem process of CO₂RR in the Ag@C@Cu NPs.

(D) Main reaction pathways of CO₂RR to C₂H₅OH and C₂H₄.

See also Figure S14.

products. Here, the main pathways from *CO to C₂H₅OH and C₂H₄ are summarized in Figure 6D.^{42–44} In pathway 1, two *CO intermediates are coupled to form *COCO, which is then reduced to *CHCHOH. Subsequently, the reaction pathways toward C₂H₅OH and C₂H₄ bifurcate, with *CHCHOH reduced to C₂H₅OH and *CCH reduced to C₂H₄. With the density functional theory (DFT) simulation, Sargent and co-workers found that a high local CO concentration could increase the coverage of *CO on the Cu surface via the Langmuir isotherm model, thus decreasing the reaction energy of the C–C coupling step.^{43,45} More importantly, a higher *CO coverage results in a lower energy barrier for the formation of *CHCHOH relative to that of *CCH because *CO occupies the adsorption sites on the Cu surface and reduces the stability of *CCH. Accordingly, the higher local CO concentration recorded for the Ag@C@Cu sample compared with the Cu sample is favorable for the production of C₂H₅OH through the *CHCHOH intermediate in pathway 1. In pathway 2, C–C coupling occurs between *CO and *CH (an intermediate derived from *CO), thus forming a *CHCO intermediate. Starting from this intermediate, the most energetically favorable pathway is through *CHCHO → *CH₂CHO → *CH₃CHO → *CH₃CH₂O and finally to the C₂H₅OH product.^{8,42,44} Although C₂H₄ can also be produced from some of these intermediates, the corresponding pathways are less favorable than the pathway for C₂H₅OH. Overall, we suggest that the improved C₂H₅OH selectivity in the tandem catalytic system can be attributed

to the enhanced *CO coverage, although advanced analytic techniques will be needed in the future to detect the involved key intermediates.

In summary, we have designed and synthesized Ag–Cu tandem catalysts with an Ag@C@Cu core-shell structure for CO₂RR. Ag@C@Cu NPs contain a thin carbon layer between the Ag core and the Cu shell to prevent the formation of an interface between Ag and Cu while still allowing CO₂ molecules to access the Ag core, thus isolating the tandem effect from other effects. We demonstrated that these catalysts can be used in flow reactors at industrially relevant current densities and that the tandem effect promoted the selectivity of C₂H₅OH relative to C₂H₄ by increasing the *CO coverage on the Cu surface. The C₂H₅OH selectivity on Ag@C@Cu can be optimized by tuning the thickness of the Cu shell. Specifically, with an Ag/Cu ratio of 0.1, we achieved 31.5% C₂H₅OH FE at -0.64 V vs RHE, corresponding to a partial current density of 126 mA cm⁻². This result suggests that a proper ratio of Ag/Cu in a tandem system is required to provide sufficient CO for C–C coupling while avoiding the excessive competition of the CO₂-to-CO reaction. The new sample-design strategies and the mechanistic insights presented in this work are expected to facilitate future studies on CO₂RR toward C₂₊ products.

EXPERIMENTAL PROCEDURES

Resource availability

Lead contact

Further information and requests for resources should be directed to and will be fulfilled by the lead contact, Wen Luo (wenluo@shu.edu.cn).

Materials availability

This study did not generate new unique reagents. All of the chemical materials and experimental procedures are provided in the [supplemental information](#).

Data and code availability

All data generated during this study are available from the [lead contact](#) upon reasonable request. The study did not generate code.

Chemicals

Silver nitrate (AgNO₃, >99.0%), L-glucose, PVP (MW = 55,000), tetraethoxysilane (TEOS), nitric acid (HNO₃), hydrazine (N₂H₄, 35 wt % aqueous solution), and deuterium (D₂O) were obtained from Sigma-Aldrich. NaOH was ordered from Reactolab S.A. and KOH was from Carl Roth. MilliQ water (18M Ω) was used to prepare electrolyte and rinse the electrode.

Synthesis of Ag NPs

Ag NPs were synthesized by reducing silver ions with glucose as reductant and PVP as surfactant in an aqueous solution at 90°C.⁴⁶ Firstly, the aqueous solution consisting of glucose (9 g), PVP (4.5 g, MW = 55,000), and 180 mL of H₂O was heated to 90°C in a round-bottom flask with a silicone oil bath and kept at 90°C for 45 min under stirring and refluxing in air. Then, the aqueous solution of AgNO₃ (2.272 M, 10.5 mL) was quickly injected into the above solution, which was then kept at 90°C for 60 min and followed with cooling in an ice bath. The reaction took place under ambient light exposure. The produced dispersion was precipitated by centrifugation (20 min, 25,160 × g) and then washed twice by water. Finally, the obtained Ag NPs were dispersed in water and stored in fridge (5°C) under dark for further use.

Synthesis of Ag@C NPs

Ag@C NPs were synthesized by carbonizing a layer of polymer wrapping on the Ag NPs. To prevent the particles from sintering during carbonization, a silica layer was grown on the polymer shell prior to carbonization.

Ag NPs were firstly coated by a layer of PDA through polymerizing free dopamine on Ag NPs.⁴⁷ The free dopamine was synthesized with the method described in a previous study.⁴⁷ Ag (59 ± 13 nm, 11.1 mg) NPs were precipitated by adding 20 mL of acetone into 9 mL of Ag NP water dispersion and then centrifuging at 7,830 RPM for 10 min. These Ag NPs were then dispersed in ethanol (60 mL). Twenty-four mg of free dopamine was added into the dispersion, which was then sonicated for 20 s to quickly dissolve the free dopamine. The dispersion was stirred for 12 h in a container with an open cap. The product, Ag@DPA NPs, was precipitated by centrifugation, washed once with ethanol, and finally dispersed in 60 mL of ethanol.

Ag@PDA NPs were further coated by SiO₂ through the hydrolysis of TEOS. 2.27 mL of water and 0.9 mL of ammonia (28 wt %) aqueous solution were added into the dispersion (60 mL) of Ag@PDA in ethanol.⁴⁸ Then, 120 μ L of TEOS were added into the dispersion under stirring. The dispersion was then stirred for 12 h at room temperature. The product denoted as Ag@PDA@SiO₂ was centrifuged, washed twice with ethanol, and finally dried under vacuum at 90°C.

Ag@PDA@SiO₂ NPs were annealed at 700°C for 1 h in N₂ in a tube furnace (at a heating rate of 5°C min⁻¹). Then, the temperature cooled naturally to room temperature. After the PDA layer in Ag@PDA@SiO₂ was carbonized, Ag@C@SiO₂ NPs were obtained.

To remove the SiO₂ layer, Ag@C@SiO₂ NPs were dispersed (0.67 mg NPs per mL) in an aqueous solution consisting of NaOH (5 mM) and dimethylamine (50 mM).⁴⁹ The dispersion was then refluxed at 70°C for 1 h under the protection of N₂. The dispersion was washed twice with ethanol and collected by centrifugation at 7,830 RPM, and the final product, Ag@C NPs, was dispersed in ethanol.

Synthesis of Ag@C@CuO and Ag@CuO

Ag@C NPs were coated with PVP in order to improve its hydrophilic. Three mL of Ag@C (1.72 mg in EtOH) was dispersed in 28.76 mL of PVP solution (10 wt %) in ethanol. The dispersion was sonicated for 10 min and then stirred for more than 10 h at room temperature. The PVP-coated Ag@C NPs were precipitated by centrifugation at 7,830 RPM for 30 min and washed twice with ethanol and finally dispersed in 3 mL of water and denoted as Ag@C@PVP NPs.

Ag@C@PVP NPs and Ag NPs were coated by a layer of Cu₂O with a controllable thickness by precipitation of Cu(OH)₂, which was then reduced by ascorbic acid. First, Ag@C@PVP NPs or Ag NPs, containing 5, 2.5, 1.7, or 0.5 mg of Ag, were dispersed in 30 mL of PVP (0.2 wt %) aqueous solution. Then, 39 μ L of Cu(NO₃)₂ (2 M) and 115.5 μ L of NH₄NO₃ (2.5 M) were added into the dispersion. After stirring for 5 min, 1.32 mL of NaOH solution (0.2 M) was dropped into the dispersion at a rate of 1.2 mL min⁻¹ controlled with a peristaltic pump. After stirring for 2 min, 2.31 mL of ascorbic-acid solution (0.1 M) was dropped into the dispersion at a rate of 0.4 mL min⁻¹. After stirring for 1 min, the NPs in the dispersion were precipitated by centrifugation, washed twice with ethanol, and finally dispersed in 3.87 mL of ethanol.

The Cu₂O layer on Ag@C@PVP@Cu₂O or Ag@Cu₂O was oxidized by the oxygen in air with the help of NH₃ H₂O. This oxidation increases the porosity and the grain-boundary density of the resulted CuO layer, which showed much better activity than Cu₂O (Figures S22 and S23). Twenty-five μ L of NH₃ H₂O aqueous solution (28 wt %) was dropped into 250 μ L of Ag@C@PVP@Cu₂O or Ag@Cu₂O dispersion in ethanol under stirring. The dispersion was stirred for another 10 min in a container with an open cap. The NPs in the dispersion were precipitated by centrifugation, washed twice with ethanol, and finally dispersed in ethanol for further use. The final products were denoted as Ag@C@CuO or Ag@CuO.

Electrochemical CO₂ reduction

Gas-diffusion electrodes were prepared by first drop casting the ink of the catalyst on the carbon paper (YLS-30T, 1.2 cm²) and then drop casting 15 μ L of Nafion solution (0.035 wt % in isopropanol). To have comparable geometric activity for Cu and Ag@C@Cu NPs, the loading of CuO was 75 μ g cm⁻², and the loading of Ag@C@CuO was 50 μ g cm⁻² (Figure 4); but for Figure 5, an equivalent Cu loading of 50 μ g cm⁻² was kept. SEM images in Figure S21 show that the NPs were scattered on the microporous layer of the gas-diffusion electrode without forming a thick catalyst layer. Strasser and co-workers found that the thickness of the catalyst layer affects the CO₂RR performance because of the CO₂ concentration and pH gradient in the catalyst layer. While the catalyst layers in our electrodes were so thin (close to one layer of NPs) that the influence from the catalyst-layer thickness was negligible.⁵⁰

The electrochemical measurements were conducted in a flow cell with the same setup described in our previous work.⁵¹ It is well known that Cu catalysts reconstruct after a relatively long reaction time, which may change the core-shell structure as reported recently.²⁴ To avoid the collapse of the core-shell structure, we conducted each reaction for 400 s. The operation protocol and the quantification of products are also described in our previous work.⁵¹

Characterization of the materials

An FEI Teneo SEM was used to observe the morphology and elemental contrast in the NPs. HRTEM images, STEM images, and EDX elemental maps were obtained by using an FEI Tecnai Osiris TEM at 200 kV. The concentration of Ag and Cu in the catalyst ink was determined by using an Agilent 5110 ICP-OES.

XRD patterns of samples were obtained using a Bruker D8 Advance instrument (40 kV, 40 mA, Cu K α radiation, λ = 0.154 nm). The XPS analysis was performed in an analysis chamber with a base pressure of 5×10^{-10} mbar equipped with a SPECS XR50-MF monochromated Al K α (1,486.61 eV) X-ray source operated at 90 W and a SPECS Phoibos 150 NAP 1D-DLD energy analyzer. XPS spectra were recorded with the fixed analyzer transmission mode using a pass energy of 20 eV for narrow scans. No charge compensation was needed as the samples were conductive. The XPS information depth of Cu 2p, Ag 3d, and C 1s photoelectrons was calculated based on their inelastic mean free path (IMFP), using QUASES-IMFP-TPP2M v.3.0 software.⁵² The information depth is calculated to be three times that of the IMFP, i.e., \sim 3.0, \sim 4.8, and \sim 9.0 nm for Cu 2p, Ag 3d, and C 1s, respectively. Raman spectra were obtained from a Renishaw inVia confocal Raman.

SUPPLEMENTAL INFORMATION

Supplemental information can be found online at <https://doi.org/10.1016/j.xcrp.2022.100949>.

ACKNOWLEDGMENTS

This research was supported by Swiss National Science Foundation (Ambizione Project no. PZ00P2_179989).

AUTHOR CONTRIBUTIONS

Conceptualization, W.L., J.Z., and A.Z.; methodology, J.Z. and W.L.; investigation, J.Z., T.H.M.P., Y.K., M.L., C.D.K., and L.Z.; resources, S.Y.; writing – original draft, J.Z. and W.L.; writing – review, T.H.M.P., Y.K., M.L., S.Y., C.D.K., L.Z., and A.Z.; writing – editing, J.Z. and W.L.; funding acquisition, W.L. and A.Z.; visualization, J.Z.; supervision, W.L. and A.Z.

DECLARATION OF INTERESTS

The authors declare no competing interests.

Received: March 2, 2022

Revised: April 24, 2022

Accepted: May 27, 2022

Published: June 17, 2022

REFERENCES

- Kibria, M.G., Edwards, J.P., Gabardo, C.M., Dinh, C.-T., Seifitokaldani, A., Sinton, D., and Sargent, E.H. (2019). Electrochemical CO₂ reduction into chemical feedstocks: from mechanistic electrocatalysis models to system design. *Adv. Mater.* 31, 1807166. <https://doi.org/10.1002/adma.201807166>.
- Karapinar, D., Creissen, C.E., Rivera de la Cruz, J.G., Schreiber, M.W., and Fontecave, M. (2021). Electrochemical CO₂ reduction to ethanol with copper-based catalysts. *ACS Energy Lett.* 6, 694–706. <https://doi.org/10.1021/acscenergylett.0c02610>.
- Nitopi, S., Bertheussen, E., Scott, S.B., Liu, X., Engstfeld, A.K., Horch, S., Seger, B., Stephens, I.E.L., Chan, K., Hahn, C., et al. (2019). Progress and perspectives of electrochemical CO₂ reduction on copper in aqueous electrolyte. *Chem. Rev.* 119, 7610–7672. <https://doi.org/10.1021/acs.chemrev.8b00705>.
- Luo, W., Xie, W., Mutschler, R., Oveisi, E., De Gregorio, G.L., Buonsanti, R., and Züttel, A. (2018). Selective and stable electroreduction of CO₂ to CO at the copper/indium interface. *ACS Catal.* 8, 6571–6581. <https://doi.org/10.1021/acscatal.7b04457>.
- Luo, W., Zhang, J., Li, M., and Züttel, A. (2019). Boosting CO production in electrocatalytic CO₂ reduction on highly porous Zn catalysts. *ACS Catal.* 9, 3783–3791. <https://doi.org/10.1021/acscatal.8b05109>.
- Birdja, Y.Y., Pérez-Gallent, E., Figueiredo, M.C., Göttle, A.J., Calle-Vallejo, F., and Koper, M.T.M. (2019). Advances and challenges in understanding the electrocatalytic conversion of carbon dioxide to fuels. *Nat. Energy* 4, 732–745. <https://doi.org/10.1038/s41560-019-0450-y>.
- Morales-Guio, C.G., Cave, E.R., Nitopi, S.A., Feaster, J.T., Wang, L., Kuhl, K.P., Jackson, A., Johnson, N.C., Abram, D.N., Hatsukade, T., et al. (2018). Improved CO₂ reduction activity towards C₂+ alcohols on a tandem gold on copper electrocatalyst. *Nat. Catal.* 1, 764–771. <https://doi.org/10.1038/s41929-018-0139-9>.
- Ren, D., Gao, J., Pan, L., Wang, Z., Luo, J., Zakeeruddin, S.M., Hagfeldt, A., and Grätzel, M. (2019). Atomic layer deposition of ZnO on CuO enables selective and efficient electroreduction of carbon dioxide to liquid fuels. *Angew. Chem. Int. Ed.* 58, 15036–15040. <https://doi.org/10.1002/anie.201909610>.
- Kuhn, A.N., Zhao, H., Nwabara, U.O., Lu, X., Liu, M., Pan, Y.-T., Zhu, W., Kenis, P.J.A., and Yang, H. (2021). Engineering silver-enriched copper core-shell electrocatalysts to enhance the production of ethylene and C₂+ chemicals from carbon dioxide at low cell potentials. *Adv. Funct. Mater.* 31, 202101668. <https://doi.org/10.1002/adfm.202101668>.
- Lee, S., Park, G., and Lee, J. (2017). Importance of Ag–Cu biphasic boundaries for selective electrochemical reduction of CO₂ to ethanol. *ACS Catal.* 7, 8594–8604. <https://doi.org/10.1021/acscatal.7b02822>.
- Li, Y.C., Wang, Z., Yuan, T., Nam, D.-H., Luo, M., Wicks, J., Chen, B., Li, J., Li, F., de Arquer, F.P.G., et al. (2019). Binding site diversity promotes CO₂ electroreduction to ethanol. *J. Am. Chem. Soc.* 141, 8584–8591. <https://doi.org/10.1021/jacs.9b02945>.
- Gao, J., Zhang, H., Guo, X., Luo, J., Zakeeruddin, S.M., Ren, D., and Grätzel, M. (2019). Selective C–C coupling in carbon dioxide electroreduction via efficient spillover of intermediates as supported by operando Raman spectroscopy. *J. Am. Chem. Soc.* 141, 18704–18714. <https://doi.org/10.1021/jacs.9b07415>.
- Huang, J., Mensi, M., Oveisi, E., Mantella, V., and Buonsanti, R. (2019). Structural sensitivities in bimetallic catalysts for electrochemical CO₂ reduction revealed by Ag–Cu nanodimers. *J. Am. Chem. Soc.* 141, 2490–2499. <https://doi.org/10.1021/jacs.8b12381>.
- Iyengar, P., Kolb, M.J., Pankhurst, J., Calle-Vallejo, F., and Buonsanti, R. (2021). Theory-guided enhancement of CO₂ reduction to ethanol on Ag–Cu tandem catalysts via particle-size effects. *ACS Catal.* 11, 13330–13336. <https://doi.org/10.1021/acscatal.1c03717>.
- Lum, Y., and Ager, J.W. (2018). Sequential catalysis controls selectivity in electrochemical CO₂ reduction on Cu. *Energy Environ. Sci.* 11, 2935–2944. <https://doi.org/10.1039/C8EE01501E>.
- Wang, J., Li, Z., Dong, C., Feng, Y., Yang, J., Liu, H., and Du, X. (2019). Silver/Copper interface for relay electroreduction of carbon dioxide to ethylene. *ACS Appl. Mater. Interfaces* 11, 2763–2767. <https://doi.org/10.1021/acsami.8b20545>.
- Xiong, L., Zhang, X., Chen, L., Deng, Z., Han, S., Chen, Y., Zhong, J., Sun, H., Lian, Y., Yang, B., et al. (2021). Geometric modulation of local CO flux in Ag@Cu₂O nanoreactors for steering the CO₂RR pathway toward high-efficacy methane production. *Adv. Mater.* 33, 2101741. <https://doi.org/10.1002/adma.202101741>.
- O'Mara, P.B., Wilde, P., Benedetti, T.M., Andronescu, C., Cheong, S., Gooding, J.J., Tilley, R.D., and Schuhmann, W. (2019). Cascade reactions in nanozymes: spatially separated active sites inside Ag–Core–Porous–Cu-shell nanoparticles for multistep carbon dioxide reduction to higher organic molecules. *J. Am. Chem. Soc.* 141, 14093–14097. <https://doi.org/10.1021/jacs.9b07310>.
- Zhang, S., Zhao, S., Qu, D., Liu, X., Wu, Y., Chen, Y., and Huang, W. (2021). Electrochemical reduction of CO₂ toward C₂ valueables on Cu@Ag core-shell tandem catalyst with tunable shell thickness. *Small* 17, 2102293. <https://doi.org/10.1002/smll.202102293>.

20. Chen, C., Li, Y., Yu, S., Louisia, S., Jin, J., Li, M., Ross, M.B., and Yang, P. (2020). Cu-Ag tandem catalysts for high-rate CO₂ electrolysis toward multicarbons. *Joule* 4, 1688–1699. <https://doi.org/10.1016/j.joule.2020.07.009>.
21. Sprunger, P.T., Lægsgaard, E., and Besenbacher, F. (1996). Growth of Ag on Cu(100) studied by STM: from surface alloying to Ag superstructures. *Phys. Rev. B* 54, 8163–8171. <https://doi.org/10.1103/PhysRevB.54.8163>.
22. Lv, X., Shang, L., Zhou, S., Li, S., Wang, Y., Wang, Z., Sham, T.-K., Peng, C., and Zheng, G. (2020). Electron-deficient Cu sites on Cu₃Ag₁ catalyst promoting CO₂ electroreduction to alcohols. *Adv. Energy Mater.* 10, 2001987. <https://doi.org/10.1002/aenm.202001987>.
23. Herzog, A., Bergmann, A., Jeon, H.S., Timoshenko, J., Kühl, S., Rettenmaier, C., Lopez Luna, M., Haase, F.T., and Roldan Cuenya, B. (2021). Operando investigation of Ag-decorated Cu₂O nanocube catalysts with enhanced CO₂ electroreduction toward liquid products. *Angew. Chem. Int. Ed.* 60, 7426–7435. <https://doi.org/10.1002/anie.202017070>.
24. Wilde, P., O'Mara, P.B., Junqueira, J.R.C., Tarnev, T., Benedetti, T.M., Andronescu, C., Chen, Y.-T., Tilley, R.D., Schuhmann, W., and Gooding, J.J. (2021). Is Cu instability during the CO₂ reduction reaction governed by the applied potential or the local CO₂ concentration? *Chem. Sci.* 12, 4028–4033. <https://doi.org/10.1039/D0SC05990K>.
25. Burdyny, T., and Smith, W.A. (2019). CO₂ reduction on gas-diffusion electrodes and why catalytic performance must be assessed at commercially-relevant conditions. *Energy Environ. Sci.* 12, 1442–1453. <https://doi.org/10.1039/C8EE03134G>.
26. Pham, T.H.M., Zhang, J., Li, M., Shen, T.-H., Ko, Y., Tileli, V., Luo, W., and Züttel, A. (2022). Enhanced electrocatalytic CO₂ reduction to C₂+ products by adjusting the local reaction environment with polymer binders. *Adv. Energy Mater.* 12, 2103663. <https://doi.org/10.1002/aenm.202103663>.
27. Zhang, J., Luo, W., and Züttel, A. (2019). Self-supported copper-based gas diffusion electrodes for CO₂ electrochemical reduction. *J. Mater. Chem.* 7, 26285–26292. <https://doi.org/10.1039/C9TA06736A>.
28. Overa, S., Ko, B.H., Zhao, Y., and Jiao, F. (2022). Electrochemical approaches for CO₂ conversion to chemicals: a journey toward practical applications. *Acc. Chem. Res.* 55, 638–648. <https://doi.org/10.1021/acs.accounts.1c00674>.
29. Zhang, Y., Li, W., Cao, Y., Chen, M., Li, W., Zai, J., Iqbal, A., Qi, R., and Qian, X. (2022). Selective electrosynthesis of 2, 5-diformylfuran in a continuous-flow system. *ChemSusChem* 15, e202102596. <https://doi.org/10.1002/cssc.202102596>.
30. Zhang, Y., Ma, D., Chen, Z., Iqbal, A., Hu, J., Chen, M., Liu, X., Tsegay, T.T., Fazal, H., Xu, P., et al. (2022). Flow electrochemistry enables microbial atmospheric CO₂ fixation via coupling with iodine-mediated organic reactions. *ACS Sustain. Chem. Eng.* 10, 541–551. <https://doi.org/10.1021/acssuschemeng.1c07037>.
31. Li, Z., Yang, Y., Yin, Z., Wei, X., Peng, H., Lyu, K., Wei, F., Xiao, L., Wang, G., Abreu, H.D., et al. (2021). Interface-enhanced catalytic selectivity on the C₂ products of CO₂ electroreduction. *ACS Catal.* 11, 2473–2482. <https://doi.org/10.1021/acscatal.0c03846>.
32. Wang, X., Wang, Z., García de Arquer, F.P., Dinh, C.-T., Ozden, A., Li, Y.C., Nam, D.-H., Li, J., Liu, Y.-S., Wicks, J., et al. (2020). Efficient electrically powered CO₂-to-ethanol via suppression of deoxygenation. *Nat. Energy* 5, 478–486. <https://doi.org/10.1038/s41560-020-0607-8>.
33. Wang, Y., Alsmeyer, D.C., and McCreery, R.L. (1990). Raman spectroscopy of carbon materials: structural basis of observed spectra. *Chem. Mater.* 2, 557–563. <https://doi.org/10.1021/cm00011a018>.
34. Feng, X., Jiang, K., Fan, S., and Kanan, M.W. (2016). A direct grain-boundary-activity correlation for CO electroreduction on Cu nanoparticles. *ACS Cent. Sci.* 2, 169–174. <https://doi.org/10.1021/acscentsci.6b00022>.
35. Lei, Q., Zhu, H., Song, K., Wei, N., Liu, L., Zhang, D., Yin, J., Dong, X., Yao, K., Wang, N., et al. (2020). Investigating the origin of enhanced C₂+ selectivity in oxide-/hydroxide-derived copper electrodes during CO₂ electroreduction. *J. Am. Chem. Soc.* 142, 4213–4222. <https://doi.org/10.1021/jacs.9b11790>.
36. Kim, Y.-G., Baricuatro, J.H., and Soriaga, M.P. (2018). Surface reconstruction of polycrystalline Cu electrodes in aqueous KHCO₃ electrolyte at potentials in the early stages of CO₂ reduction. *Electrocatalysis* 9, 526–530. <https://doi.org/10.1007/s12678-018-0469-z>.
37. Möller, T., Scholten, F., Thanh, T.N., Sinev, I., Timoshenko, J., Wang, X., Jovanov, Z., Gliech, M., Roldan Cuenya, B., Varela, A.S., and Strasser, P. (2020). Electrocatalytic CO₂ reduction on CuO_x nanocubes: tracking the evolution of chemical state, geometric structure, and catalytic selectivity using operando spectroscopy. *Angew. Chem. Int. Ed.* 59, 17974–17983. <https://doi.org/10.1002/anie.202007136>.
38. Simon, G.H., Kley, C.S., and Roldan Cuenya, B. (2021). Potential-dependent morphology of copper catalysts during CO₂ electroreduction revealed by in situ atomic force microscopy. *Angew. Chem. Int. Ed.* 60, 2561–2568. <https://doi.org/10.1002/anie.202010449>.
39. Yang, C., Ko, B.H., Hwang, S., Liu, Z., Yao, Y., Luc, W., Cui, M., Malkani, A.S., Li, T., Wang, X., et al. (2020). Overcoming immiscibility toward bimetallic catalyst library. *Sci. Adv.* 6, eaaz6844. <https://doi.org/10.1126/sciadv.aaz6844>.
40. Zhong, Y., Kong, X., Song, Z., Liu, Y., Peng, L., Zhang, L., Luo, X., Zeng, J., and Geng, Z. (2022). Adjusting local CO confinement in porous-shell Ag@Cu catalysts for enhancing C–C coupling toward CO₂ electroreduction. *Nano Lett.* 22, 2554–2560. <https://doi.org/10.1021/acs.nanolett.1c04815>.
41. Kim, D., Resasco, J., Yu, Y., Asiri, A.M., and Yang, P. (2014). Synergistic geometric and electronic effects for electrochemical reduction of carbon dioxide using gold–copper bimetallic nanoparticles. *Nat. Commun.* 5, 4948. <https://doi.org/10.1038/ncomms5948>.
42. Iyengar, P., Kolb, M.J., Pankhurst, J.R., Calle-Vallejo, F., and Buonsanti, R. (2021). Elucidating the facet-dependent selectivity for CO₂ electroreduction to ethanol of Cu–Ag tandem catalysts. *ACS Catal.* 11, 4456–4463. <https://doi.org/10.1021/acscatal.1c00420>.
43. Li, J., Wang, Z., McCallum, C., Xu, Y., Li, F., Wang, Y., Gabardo, C.M., Dinh, C.-T., Zhuang, T.-T., Wang, L., et al. (2019). Constraining CO coverage on copper promotes high-efficiency ethylene electroproduction. *Nat. Catal.* 2, 1124–1131. <https://doi.org/10.1038/s41929-019-0380-x>.
44. Ting, L.R.L., Piqué, O., Lim, S.Y., Tanhaei, M., Calle-Vallejo, F., and Yeo, B.S. (2020). Enhancing CO₂ electroreduction to ethanol on copper–silver composites by opening an alternative catalytic pathway. *ACS Catal.* 10, 4059–4069. <https://doi.org/10.1021/acscatal.9b05319>.
45. Li, F., Li, Y.C., Wang, Z., Li, J., Nam, D.-H., Lum, Y., Luo, M., Wang, X., Ozden, A., Hung, S.-F., et al. (2020). Cooperative CO₂-to-ethanol conversion via enriched intermediates at molecule–metal catalyst interfaces. *Nat. Catal.* 3, 75–82. <https://doi.org/10.1038/s41929-019-0383-7>.
46. Banerjee, S., Loza, K., Meyer-Zaika, W., Prymak, O., and Eppel, M. (2014). Structural evolution of silver nanoparticles during wet-chemical synthesis. *Chem. Mater.* 26, 951–957. <https://doi.org/10.1021/cm4025342>.
47. Yang, S., Peng, L., Sun, D.T., Asgari, M., Oveis, E., Trukhina, O., Bulut, S., Jamali, A., and Queen, W.L. (2019). A new post-synthetic polymerization strategy makes metal–organic frameworks more stable. *Chem. Sci.* 10, 4542–4549. <https://doi.org/10.1039/C9SC00135B>.
48. Bai, Z., Chen, R., Si, P., Huang, Y., Sun, H., and Kim, D.-H. (2013). Fluorescent pH sensor based on Ag@SiO₂ core–shell nanoparticle. *ACS Appl. Mater. Interfaces* 5, 5856–5860. <https://doi.org/10.1021/am401528w>.
49. Gao, C., Zhang, Q., Lu, Z., and Yin, Y. (2011). Templated synthesis of metal nanorods in silica nanotubes. *J. Am. Chem. Soc.* 133, 19706–19709. <https://doi.org/10.1021/ja209647d>.
50. Möller, T., Ngo Thanh, T., Wang, X., Ju, W., Jovanov, Z., and Strasser, P. (2021). The product selectivity zones in gas diffusion electrodes during the electrocatalytic reduction of CO₂. *Energy Environ. Sci.* 14, 5995–6006. <https://doi.org/10.1039/D1EE01696B>.
51. Zhang, J., Luo, W., and Züttel, A. (2020). Crossover of liquid products from electrochemical CO₂ reduction through gas diffusion electrode and anion exchange membrane. *Catal. Sci.* 385, 140–145. <https://doi.org/10.1016/j.jcat.2020.03.013>.
52. Tanuma, S., Powell, C.J., and Penn, D.R. (1991). Calculations of electron inelastic mean free paths. II. Data for 27 elements over the 50–2000 eV range. *Surf. Interface Anal.* 17, 911–926. <https://doi.org/10.1002/sia.740171304>.